
Article:
Paddock, R. W., von der Leyen, M. W., Aboushelbaya, R. et al. (27 more authors) (2023) Measuring the principal Hugoniot of inertial-confinement-fusion-relevant TMPTA plastic foams. Physical Review E. 025206. ISSN 1550-2376

https://doi.org/10.1103/PhysRevE.107.025206

Measuring the principal Hugoniot of inertial-confinement-fusion-relevant TMPTA plastic foams

R. W. Paddock,* M. W. von der Leyen, R. Aboushelbaya, and P. A. Norreys†
Department of Physics, Atomic and Laser Physics Sub-Department, Clarendon Laboratory, University of Oxford, Parks Road, Oxford, OX1 3PU, United Kingdom

D. J. Chapman and D. E. Eakins
Department of Engineering Science, University of Oxford, Oxford OX1 3PJ, United Kingdom

M. Oliver, R. J. Clarke, M. Notley, C. D. Baird, N. Booth, C. Spindloe, D. Haddock, S. Irving, and R. H. H. Scott
Central Laser Facility, STFC, Rutherford Appleton Laboratory, Harwell Campus, Didcot OX11 0QX, United Kingdom

J. Pasley
York Plasma Institute, School of Physics, Electronics and Technology, University of York, York YO10 5DD, United Kingdom

M. Cipriani and F. Consoli
ENEA, Fusion and Technology for Nuclear Safety and Security Department, C.R.Frascati, via E. Fermi 45, 00044 Frascati, Rome, Italy

B. Albertazzi and M. Koenig
LULI - CNRS, CEA, Sorbonne Universités, Ecole Polytechnique, Institut Polytechnique de Paris–F-91120 Palaiseau cedex, France

A. S. Martynenko, L. Wegert, and P. Neumayer
GSI Helmholtzzentrum für Schwerionenforschung, Planckstraße 1, 64291 Darmstadt, Germany

P. Tchórz and P. Rączka
Institute of Plasma Physics and Laser Microfusion, 01-497 Warsaw, Poland

P. Mabey
Department of Physics, Freie Universität Berlin, Arnimallee 14, 14195 Berlin, Germany

W. Garbett
AWE plc, Aldermaston, Reading, Berkshire RG7 4PR, United Kingdom

R. M. N. Goshadze, V. V. Karasiev, and S. X. Hu
Laboratory for Laser Energetics, University of Rochester, Rochester, New York 14623, USA

(Received 7 October 2022; accepted 9 December 2022; published 23 February 2023)

Wetted-foam layers are of significant interest for inertial-confinement-fusion capsules, due to the control they provide over the convergence ratio of the implosion and the opportunity this affords to minimize hydrodynamic instability growth. However, the equation of state for fusion-relevant foams are not well characterized, and many simulations rely on modeling such foams as a homogeneous medium with the foam average density. To address this issue, an experiment was performed using the VULCAN Nd:glass laser at the Central Laser Facility. The aim was to measure the principal Hugoniot of TMPTA plastic foams at 260 mg/cm^3, corresponding to the density of liquid DT-wetted-foam layers, and their "hydrodynamic equivalent" capsules. A VISAR was used to obtain the shock velocity of both the foam and an α-quartz reference layer, while streaked optical pyrometry provided the temperature of the shocked material. The measurements confirm that, for the 20–120 GPa pressure range accessed, this material can indeed be well described using the equation of state of the homogeneous medium at the foam density.

DOI: 10.1103/PhysRevE.107.025206

*robert.paddock@physics.ox.ac.uk
†Also at John Adams Institute for Accelerator Science, University of Oxford, Denys Wilkinson Building, Keble Road, Oxford OX1 3RH, United Kingdom.

I. INTRODUCTION

Foams are of broad interest for inertial-confinement-fusion (ICF) research for a number of reasons, including (but not limited to) laser beam smoothing and imprint mitigation [1,2], adiabat shaping [3–5], increasing absorption of Nd-laser light [6], and increasing conversion from laser light into x rays [7]. One particularly interesting application is the use of deuterium-tritium (DT) wetted-foam layers, which can be used in place of conventional DT-ice layers in ICF capsules. These wetted-foam or "liquid-layer" capsules can be fielded at a range of higher initial temperatures, which leads to a range of vapor pressures within the capsule and allows a useful degree of control over the convergence (or amount of compression) that the capsule undergoes [8]. Recent experiments at the National Ignition Facility investigating these implosions have demonstrated good performance and low-instability growth [8,9], which has led to further interest in the potential of these target designs [10–13]. Novel "dynamic-shell" designs, in which a low-density hotspot and high-density shell are formed dynamically in a capsule consisting of liquid-DT and wetted-foam layers, have also recently been developed [14].

In spite of this interest, simulating foams in radiation hydrodynamics codes remains a challenging problem, with the impact of homogenisation and microstructure still areas of active research [15–18]. One issue of key importance is the foam equation of state (EOS). For DT wetted-foams it is known that (for currently achievable foam densities) a mixed CH+DT equation of state is required [10]. However, the EOS of even dry (i.e., without DT-wetting) foams, which are used for this mixed-EOS, are not well characterised. Foams are commonly simulated as an equivalent homogeneous material, where they are treated as a low-density version of the material (usually plastic) of which they are composed, without accounting for the foam structure—yet this approach has previously proven to be inadequate in the modeling of some experiments [19]. This is therefore a source of potential uncertainty for designs involving foam materials and needs to be addressed. A number of previous experiments have explored the Hugoniot and shock temperatures for foams of a range of compositions and densities for a range of different shock strengths [e.g., Refs. [20–25]], but there is a continuing need for more data on this subject.

This paper describes a recent experiment using the VULCAN kJ-class Nd:glass laser at the UKRI-STFC Rutherford Appleton Laboratory to investigate the EOS of one such material. Experimental measurements of the principal Hugoniot of trimethylolpropane triacrylate foam ("TMPTA," $C_{15}H_{12}O_6$) are presented and compared to theoretical Hugoniots generated from different EOS models for homogeneous TMPTA and polystyrene (CH). The pore size of this foam is around 1 μm. A foam density of 260 mg/cm^3 was used, which is of direct interest for recently proposed "hydrodynamic equivalent" ICF capsules [26]. These capsules have been proposed as room-temperature surrogates for liquid DT-wetted-foam designs; a dry foam of 253 mg/cm^3 density is used in place of the 253 mg/cm^3 wetted-foam layer, giving a capsule with comparable hydrodynamic performance (but reduced yield) without the need for cryogenic cooling. Improving the equation of state models of these foam materials will also be of use in developing more accurate equation of state models for wetted foams (although the foam itself in such layers has a much lower density of around 25 mg/cm^3 [27,28]).

The experiment used VISAR [29] to measure the average shock velocity in the foam and an α-quartz reference layer for each shot, which enabled an impedance matching calculation to be performed to calculate the full shock state of the foam. Streaked optical pyrometry (SOP) was also used to infer the foam shock-temperature. This paper is organized as follows. Full details of the target design, experimental procedure, and setup are given in Sec. II. Section III provides details of the impedance matching and gray-body temperature calculations performed on the experimental results. Section IV looks at the resulting data, and compares these to both theoretical models and data from other facilities on various foams with varying initial densities. Section V summarizes the results and concludes the paper.

II. EXPERIMENT

The VULCAN laser was used to drive a shock-wave through a multilayer "step" target, while VISAR and SOP diagnostics measured the shock-behavior of the rear two layers. A simple schematic of the setup is shown in Fig. 1, with a closer view of the target and beams shown in Fig. 2. The six laser beams (the only VULCAN beams used in this experiment) were positioned in three planes at -25°, 0°, and 25° with respect to the horizontal, with two beams within each plane at 6° and -6° to the target normal. Random phase plates were used to produce a "flat-topped" focal spot with a uniform intensity over 400 μm on the front surface of the target. The beams were frequency doubled to 527 nm, and were overlapped to produce a single "top hat" temporal pulse. The length of this pulse was varied between 2 ns and 9 ns over the course of the experiment (with around 500 ps rise and decay time either side of the peak power). The total pulse energy varied between approximately 300 and 700 J, giving intensities on target between 3×10^{13} and 2×10^{14} W/cm^2. An x-ray pinhole camera (not displayed in the schematic) imaged the front surface of the target, and was used to confirm the diameter of the focal spot along with positioning and overlap of the beams.

The target design displayed in Fig. 2 consists of four layers: an ∼40 μm CH ablator, followed by an ∼3 μm gold layer, an ∼40 μm α-quartz reference layer, and then finally the ∼40 μm TMPTA foam. The laser pulses were incident upon the ablator layer, generating a shock wave which was roughly uniform over the 400 μm focal spot. The gold layer was present to absorb any x rays that were generated in the coronal plasma during the laser-plasma interaction, and thus prevent x-ray preheating of the quartz and foam. The α-quartz was a reference material for the impedance matching and SOP. The foam layer covered only half of the rear side of the target. This multilayer "step" target design was similar to those used in previous experiments to investigate other materials [21,22], and allowed diagnostic line-of-sight to both the quartz and foam layers. There were no glue layers present in the bulk of the target; the CH ablator and gold layers were deposited directly onto the quartz without glue, while the foam was tacked to the quartz at the corners only (which were outside of

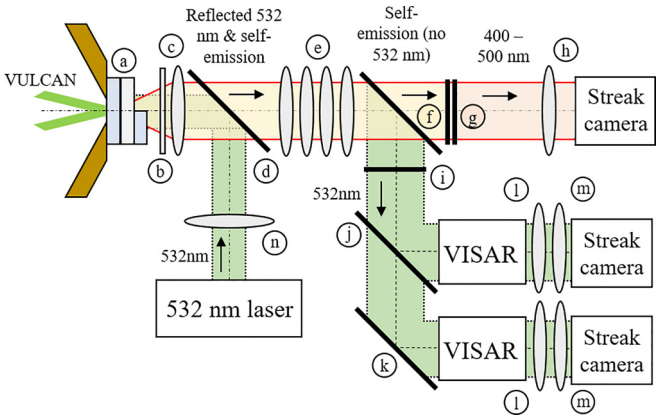

FIG. 1. A simplified schematic of the experiment. The routes of different frequencies are indicated, while key components are labeled. A 532 nm laser is passed through a beamsplitter (d) through the objective lens ((c), protected by a blast shield (b)) onto the target ((a), as detailed in Fig. 2). The lens (n) with a focal length of 400 mm forms a lens pair with (c), such that the probe beam is collimated at the target (rather than focussed by (c)). The reflected 532 nm light and self-emission is collected by the objective lens, and passes through a system of 4 lenses (e), with focal lengths of 700, 500, 700, and 250 mm. A dichroic mirror (f) separates a narrow band of wavelengths around 532 nm from the transmitted light. Filters (g) leave only the 400–500 nm light, which is focused by a $f = 300$ mm lens (h) into a streak camera, forming the SOP system. The 532 nm light is further isolated by a notch filter (i), removing any 527 nm noise from VULCAN. A beamsplitter (j) directs the light into two VISAR systems, with different etalon lengths. (k) is a simple turning mirror. Finally, a $f = 300$ mm lens (l) focuses the light from each of these into a separate streak camera, while a $f = 200$ mm cylindrical lens (m) focuses it further in the dimension perpendicular to the streak camera slit to improve signal strength. The schematic is not to scale, and additional components (such as turning mirrors) have not been displayed.

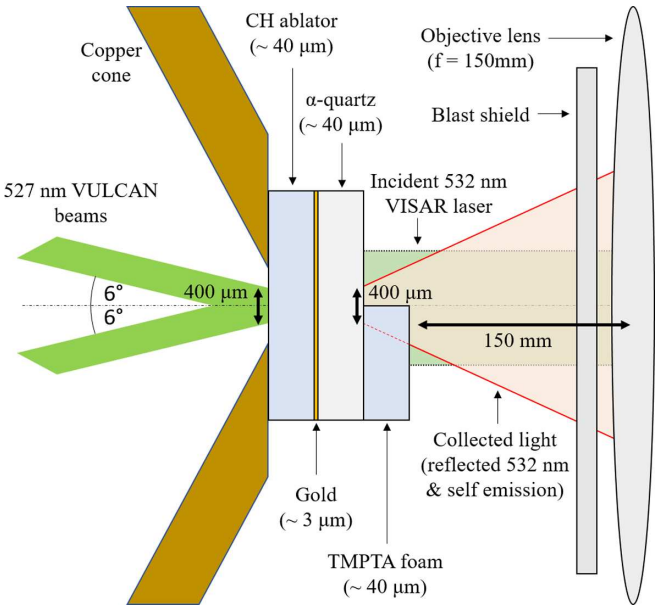

FIG. 2. Simple schematic showing the target and objective lens (top view, not to scale).

the 400 μm region of interest, as the transverse dimensions of the foam were around 1 mm). Each target was metrologized to provide precise thickness measurements of the different layer materials and to confirm preshot homogeneity on a shot-by-shot basis.

VISAR and SOP diagnostics measured the shock breakout and self-emission from the quartz and foam layers. A 532 nm laser was used to drive the VISAR, and provided a single 20 ns pulse timed to overlap the VULCAN pulse and shock breakouts. The diagnostic laser (with a beam diameter of roughly 1 mm) was reflected from the rear surface of the target. The reflected 532 nm light, along with the self-emission from the target, was collected by a 150 mm objective lens (with a blast shield used to protect the lens from debris). A further four lenses (with focal lengths of 700, 500, 700, and 250 mm) were used to relay this collected light and provide magnification. All lenses used in this relay were achromatic doublets. A dichroic mirror reflected out the 532 nm reflected laser light into the VISAR system, with a notch filter being used to further isolate the 532 nm light from any 527 nm VULCAN light. Two VISARs were used to provide two independent measurements, with different etalon lengths to allow for unambiguous velocity determination. Cylindrical lenses were used to increase the signal intensity on the corresponding streak cameras. The self-emission passed through the dichroic mirror, was filtered down so that only the 400–500 nm range remained, and was focused by an $f = 300$ mm lens into a streak camera to form the SOP system. The shared imaging system meant that the VISAR and SOP were co-aligned (though differences in the streak cameras, plus additional lenses within the VISAR, meant that the magnification/field of view differed). The system was aligned so that both the diagnostics and the shock were centered on the quartz-foam step, so that the shock state in both quartz and foam could be measured.

III. DATA ANALYSIS

A. VISAR analysis and impedance matching

Raw VISAR data from a typical shot is presented in Fig. 3. The left half of the image corresponds to signal from the quartz, while the right side corresponds to the signal from the foam. The key shock timings can be identified: first, the shock enters the quartz (seen as a change in signal intensity on the left), before breaking out of the quartz rear surface (fringe extinction, left) and entering the foam, before finally breaking out of the foam rear surface (extinction, right). The shock transit time through both the quartz and foam layers could therefore be determined which, using the known layer thicknesses, enabled calculation of the average shock velocity in the two materials.

α-quartz is commonly used for shock EOS experiments because, when shocked to above ~100 GPa, it becomes a conductive fluid with significant reflectivity [30]. When such pressures are achieved the diagnostic laser pulse will reflect directly from the moving shock front, causing a fringe shift in the VISAR data which is used to calculate the shock velocity as a function of time [31]. Unfortunately, for most shots in this experiment (and as seen in Fig. 3) no obvious fringe shift was

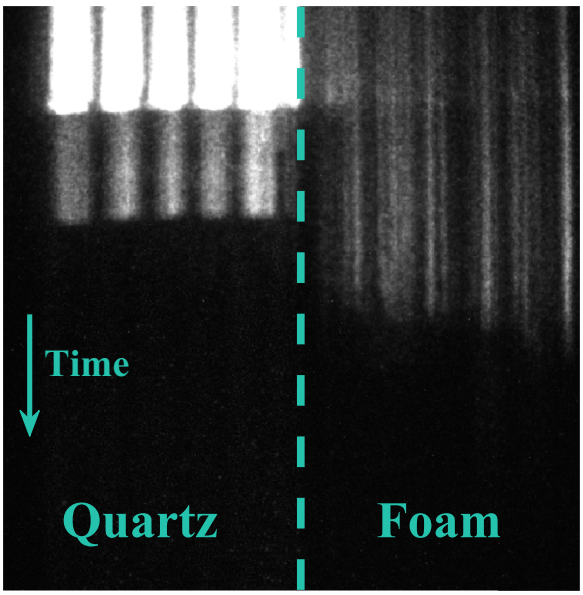

FIG. 3. Raw VISAR data (20 ns streak time). The left half of the image corresponds to signal from the quartz, while the right side corresponds to the foam. Timings for shock entry into the quartz (change in signal strength on the left), shock breakout from the quartz (extinction of signal on left) and shock breakout from the foam (extinction of signal on right) can all be identified.

observed, despite the fact that 1D simulations suggested that the shock pressure should be sufficient for this to occur. The reason for this is discussed in Sec. IV C. This meant that the average velocity calculated from the shock breakout timings was used instead.

The determined quartz and foam shock velocities were then used in the impedance matching procedure outlined by Knudson and Desjarlais [32] to calculate the foam shock state achieved in each shot. This calculation, described below, uses the Rankine-Hugoniot equations:

$$(E - E_0) = P(V_0 - V)/2, \tag{1}$$

$$P = \rho_0 U_s u_p, \tag{2}$$

$$\rho = \rho_0 U_s/(U_s - u_p), \tag{3}$$

where E, P, V, U_s, u_p, and ρ are internal energy, pressure, specific volume, shock velocity, particle velocity, and density, respectively [33]. Variables with a subscript "0" describe the state of the unshocked material ahead of the shock front, while those without a subscript describe the shocked material behind this shock front (the pressure of the unshocked material, P_0, is assumed to be 0 and has thus been omitted). These relations are derived based on conservation of energy, mass, and momentum across the front of a shock, and apply in any material. In this paper, the superscripts "quartz" and "foam" will be used to indicate where a measured/calculated value for a particular material is being used.

First, the known α-quartz Hugoniot is used along with the measured quartz velocity, U_s^{quartz} to identify the state of the shocked quartz. The Hugoniot used was of the form

TABLE I. Coefficients for the quartz Hugoniot in Eq. (4), reproduced from Ref. [32].

a_0 (km/s)	a_1	a_2 (km/s)$^{-1}$	a_3 (km/s)$^{-2}$
1.754	1.862	-3.364×10^{-2}	5.666×10^{-4}

$$U_s = \sum_{n=0}^{3} a_n u_p^n, \tag{4}$$

with coefficients in Table I [32], and is a cubic fit to experimental data from Ref. [34]. Equation (2) is used to convert this Hugoniot into the (u_p, P) plane. Equation (2) is also used to calculate the Rayleigh line, an additional constraint on the shocked quartz in the (u_p, P) plane; the measured shock velocity of the quartz, U_s^{quartz}, is substituted into this equation to produce a chord upon which the shocked quartz state must sit, $P = \rho_0^{\text{quartz}} U_s^{\text{quartz}} u_p$. The shocked quartz state in the experiment must satisfy both the Rayleigh line and the Hugoniot, and can thus be identified as the intercept of these two curves in the (u_p, P) plane. This is shown in Fig. 4 (along with additional curves for the following steps).

When the shock crosses the interface between the quartz and the lower-impedance foam, a rarefaction wave propagates back through the quartz causing it to relax. The release isentrope describes the locus of possible states that the quartz can relax to from a given shock state. It is calculated here according to the method presented in Knudson and Desjarlais [32], but with a small variation. They use a new "linear-reference" Mie-Grüneisen model with a variable Grüneisen parameter, but this model is not valid over the range of shock velocities

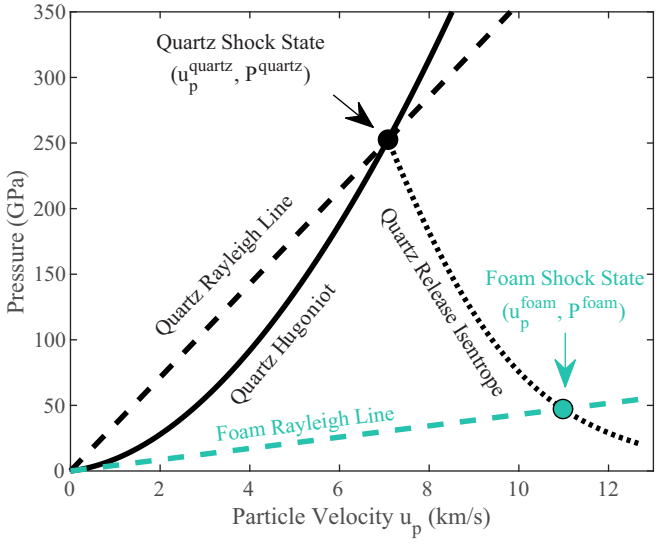

FIG. 4. The impedance matching calculation for the data from Fig. 3, shown graphically. The intercept of the known quartz Hugoniot and the quartz Rayleigh line (defined by the measured quartz shock velocity) provides the shocked quartz state. This is used to calculate the appropriate quartz release isentrope. The intercept of this with the foam Rayleigh line provides the foam shock state.

measured in this paper. A conventional Mie-Grüneisen model with a fixed Grüneisen parameter of $\Gamma = 0.64$ was therefore used instead for this analysis. This value of the Grüneisen parameter was calculated from a range of EOS models [35], and is in good agreement with that derived [35] from experiments [36,37].

The "impedance matching" aspect of the calculation is introduced by the fact that particle velocity and pressure is conserved across the interface between the two materials [38], meaning that the value of these variables is shared between the shocked foam and relaxed quartz. The range of possible relaxed quartz states is defined by the isentrope. The experimentally measured foam shock velocity, U_s^{foam}, defines the foam Rayleigh line, $P = \rho_0^{\text{foam}} U_s^{\text{foam}} u_p$. The shared particle velocity and pressure is therefore identified from the intercept of these two curves. P^{foam} and u_p^{foam} (determined from this intercept) and U_s^{foam} (measured) are then used to calculate all variables for the shocked foam using the Rankine-Hugoniot relations. This defines the foam shock state achieved in a single shot where the quartz and foam shock velocities were measured; by repeating this calculation for a number of shots, Hugoniot data for a wider range of shock velocities is produced.

The uncertainty in this calculation was quantified using a Monte Carlo approach [39]. The measured values and uncertainties of the different quantities (shock velocities, densities, and layer thicknesses) were considered to be the mean and standard deviations of normal distributions. Ten thousand iterations of the above calculation were run for each shot, sampling different values from these distributions each time. Uncertainty in the α-quartz Hugoniot in Eq. (4) was also included, by using 10 000 samples of the Hugoniot coefficients in place of those in Table I using the corresponding covariance matrix [32]. This produced a distribution of values for each shock variable of the foam. The standard deviation around the mean of this distribution was used to define the range of possible uncertainty. A selection of these distributions are displayed in Fig. 5.

The resulting distributions are not normal, and as a result the distribution mean may differ from the value obtained from the "exact" impedance matching calculation displayed in Fig. 4 (which does not factor in the uncertainties). To ensure consistency (i.e., so that when the quartz shock velocities and pressures are quoted together, they are exactly compatible with the Hugoniot from which they are derived), the values used in the figures and tables in later sections of this paper are those obtained from the "exact" calculation. However, the standard deviation which defines the uncertainty range is centered on the mean of the distribution—and thus the quoted errors in later sections are asymmetrical, accounting for this difference between the quoted and mean values.

B. SOP analysis

Streaked optical pyrometry allows for the calculation of the temperature of a body, by comparing the surface brightness of that body in a narrow wavelength band with the brightness produced by a perfect black-body [33], assuming that the shocked material is optically thick to the wavelength band used. A "gray-body" approximation provides a more accurate

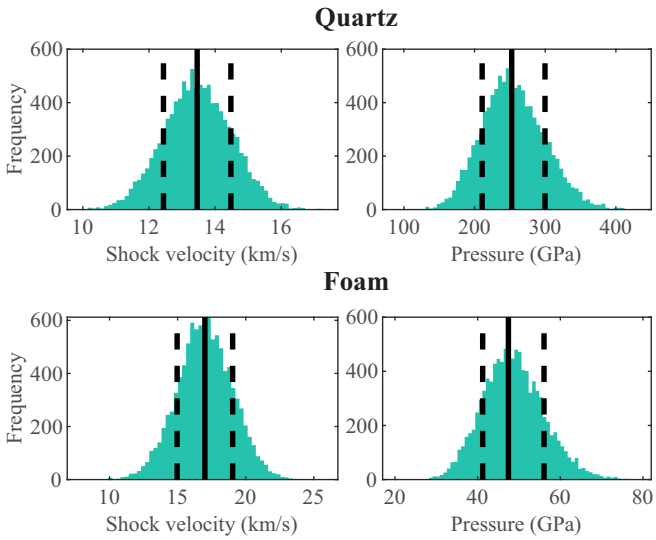

FIG. 5. Histograms of the shock velocity and pressure distributions (for both quartz and foam) used in the Monte Carlo analysis. For the shock velocities, the experimentally measured values (solid lines) and experimental uncertainty (dashed lines) were used as the means and standard deviations of uniform distributions. These were each randomly sampled 10 000 times, along with the other measured quantities, and the impedance matching calculation performed for each set of samples. This resulted in distributions for each of the calculated quantities, such as the pressure. The standard deviation (dashed lines) around the mean of each of these resulting distributions were then calculated, and used as the uncertainty of that shock variable (the actual value was obtained from an impedance match calculation of each value without error—the solid black line on the two pressure distributions).

calculation, by accounting for the emissivity of the surface [40]. The gray-body temperature T of the material can be calculated from the measured SOP intensity I,

$$T = \frac{T_0}{\ln\left[1 + \frac{(1-R)A}{I}\right]}, \tag{5}$$

where R is the reflectivity of the shocked material and $T_0 = hc/\lambda_0$ is a constant calculated from Planck's constant h, the speed of light c, and the central wavelength of the frequency band λ_0 (for the 400–500 nm band used in this experiment, $\lambda_0 = 450$ nm). A is a calibration constant for the SOP system [41], which must be determined. The SOP was not absolutely calibrated (due to a lack of calibrated white light source), and so it was effectively calibrated each time on-shot by using the shocked quartz as a reference of known temperature [42].

Raw SOP data (corresponding to the same shot as the VISAR data in Fig. 3) is shown in Fig. 6. There are two broad bands of signal—an earlier one on the left side of the image corresponding to self-emission from the quartz, and a later one on the right corresponding to the foam. The spatial region over which each band was roughly uniform was selected, and averaged to give mean counts (on the streak camera) versus time. The regions used for the averages correspond to the boxes in Fig. 6, while the spatially averaged signal is shown as the trace on the figure. A large peak can be seen for the quartz

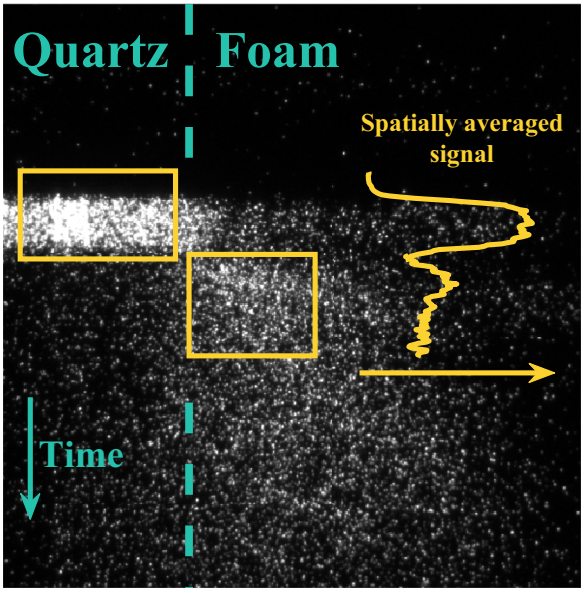

FIG. 6. Raw SOP data (50 ns streak time). Quartz emission is detected first on the left side of the image, followed by foam emission on the right side at a later time. Regions containing the SOP signal for the quartz and foam were selected (boxes), and the signal in these regions were spatially averaged to give the mean signal from the material as a function of time (trace on image).

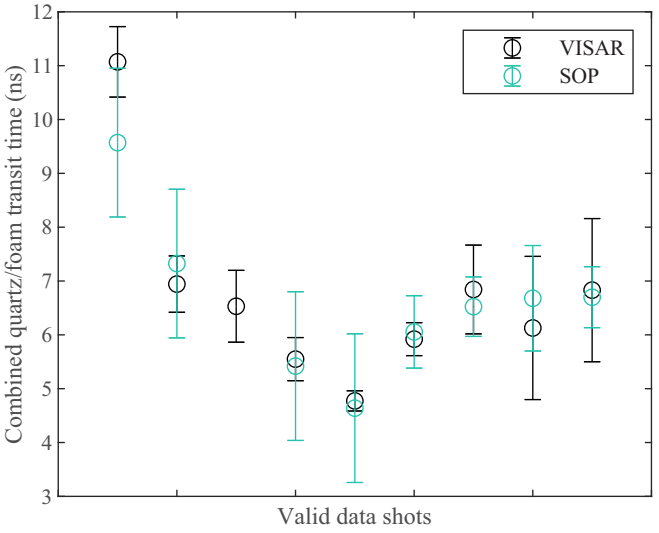

FIG. 7. Combined quartz and foam transit times, as determined for each valid data shot from the VISAR and SOP. All shots agree to within the error (which is due to uncertainty in identifying the relevant behaviors in the raw data, and the finite slit width of the streak cameras).

signal, followed by a small (but distinct) peak from the foam emission.

An expression for quartz reflectivity as a function of shock velocity is provided in Ref. [42]. The reflectivity relationship for the TMPTA foam was estimated using previously published density functional theory (DFT) data for polystyrene plastic [43], combined with new DFT simulations for the material in this experiment using the same method [43,44]. DFT simulations were used to calculate the reflectivity of shocked TMPTA foam at two relevant pressures (50 and 150 GPa), and the CH reflectivity data (which was linearly extrapolated to apply at lower pressures) was then scaled and linearly shifted to pass through both of these points. The required reflectivity R for both materials could thus be calculated, as required for the gray-body calculation. To perform the calibration, the expected quartz shock temperature was calculated based on the VISAR-measured shock velocity, using the expression given in Ref. [42] (a power-law fit to data from Ref. [30]). By substituting this temperature and the maximum SOP intensity from the quartz into Eq. (5), it was possible to calculate the calibration constant A for the shot. This therefore allowed the foam temperature T from that shot to also be calculated. This calculation was performed in parallel with the VISAR analysis described above, and the error was also calculated using MC simulation. The uncertainty in the shock velocities, and that arising from the use of fits for quartz temperature and quartz and foam reflectivities (for which uncertainties were estimated) resulted in a large overall uncertainty for this calculation.

Shock entry into the quartz can be identified from the SOP data by the start of the quartz signal (since the shocked quartz is transparent to the thermal radiation). The shock breakout from the foam can also be roughly identified from the peak of the foam signal (the foam is much less transparent, so there is only some low emission just before this time). However, there is no clearly identifiable change in the data corresponding to the shock leaving the quartz and entering the foam, which prevents the transit times (and thus shock velocities) in the two materials from being calculated. However, a combined quartz and foam transit time can be determined, which can be compared with the VISAR data to check for consistency. This is done in Fig. 7, which demonstrates good agreement between the two diagnostics. This increased confidence in both the results, and also in the SOP data; while the foam SOP signal is weak, the fact that the timing of the signal agrees with the VISAR timing data suggests that it is indeed a physical signal and is not merely background noise.

C. Shot selection

A number of shots provided VISAR images where the breakout signals were not fully clear, due to signal strength issues. For shots to be included in the analysis all three shock breakout signals had to be identifiable with reasonable confidence. A small number of shots also displayed two distinct regions of SOP emission in the quartz, which was sometimes also accompanied by an increase in intensity in the VISAR signal. The most likely explanation for this behavior is a second shock overtaking the first within the quartz. This behavior was observed in some 1D simulations of the experiment, although it was not possible to accurately predict on which shots it would occur (particularly as the passage of the first shock would magnify the uncertainty in predicting the second). Such a phenomena would mean that the average shock velocity would contain information from two distinct shocks traveling at different speeds, and would therefore not be a good description of the shock at the time it crossed the quartz-foam

TABLE II. Principal Hugoniot data for the compressed foam. U_s^{quartz} and U_s^{foam} are the measured quartz and foam shock velocities. The quartz particle velocity, pressure, and temperature (u_p^{quartz}, P^{quartz}, and T^{quartz}) are not directly measured, and are instead calculated from the shock velocity using known relations (the Hugoniot [32], and a measured relationship between U_s^{quartz} and T^{quartz} [42]). u_p^{foam} and P^{foam} are the foam particle velocity and pressure, determined from the impedance matching calculation, while T^{foam} is the foam gray-body temperature calculated in the SOP analysis. Other than U_s^{quartz} and U_s^{foam}, where the quoted error is the experimental uncertainty, the errors given for each value are the standard deviation of a distribution for that value obtained from 10 000 random Monte Carlo iterations. The SOP did not work correctly on all shots, hence the missing T^{foam} values.

U_s^{quartz} (km/s)	u_p^{quartz} (km/s)	P^{quartz} (GPa)	T^{quartz} (eV)	U_s^{foam} (km/s)	u_p^{foam} (km/s)	P^{foam} (GPa)	T^{foam} (eV)
9.2 ± 0.6	$4.3^{+0.4}_{-0.4}$	106^{+17}_{-16}	–	11.1 ± 1.1	$6.8^{+0.6}_{-0.7}$	$19.2^{+3.0}_{-2.1}$	–
13.4 ± 2.4	$7.0^{+1.8}_{-1.6}$	249^{+123}_{-93}	$0.96^{+0.59}_{-0.40}$	15.9 ± 4.9	$11.1^{+3.2}_{-2.8}$	$44.4^{+19.3}_{-16.0}$	$0.60^{+0.30}_{-0.23}$
13.4 ± 0.4	$7.0^{+0.2}_{-0.2}$	250^{+16}_{-15}	–	22.3 ± 3.5	$10.5^{+0.5}_{-0.5}$	$59.0^{+9.9}_{-7.3}$	–
13.5 ± 1.0	$7.1^{+0.7}_{-0.7}$	253^{+47}_{-42}	$0.98^{+0.21}_{-0.18}$	17.0 ± 2.0	$11.0^{+1.2}_{-1.2}$	$47.4^{+8.6}_{-6.2}$	$0.62^{+0.16}_{-0.13}$
14.3 ± 1.5	$7.7^{+1.0}_{-1.0}$	290^{+73}_{-64}	$1.14^{+0.35}_{-0.28}$	16.3 ± 2.7	$12.1^{+1.9}_{-1.8}$	$50.0^{+12.0}_{-9.4}$	$0.68^{+0.20}_{-0.17}$
14.4 ± 2.7	$7.7^{+2.0}_{-1.9}$	296^{+150}_{-117}	$1.17^{+0.76}_{-0.53}$	14.5 ± 3.3	$12.5^{+3.7}_{-3.3}$	$45.7^{+17.9}_{-14.8}$	$0.69^{+0.35}_{-0.28}$
15.7 ± 1.8	$8.7^{+1.3}_{-1.2}$	362^{+102}_{-87}	–	25.2 ± 2.8	$13.0^{+2.2}_{-2.1}$	$82.9^{+18.8}_{-13.9}$	–
16.9 ± 1.1	$9.5^{+0.8}_{-0.8}$	423^{+69}_{-62}	$1.79^{+0.36}_{-0.31}$	19.0 ± 2.5	$15.1^{+1.5}_{-1.5}$	$72.3^{+13.2}_{-9.6}$	$1.29^{+0.31}_{-0.24}$
21.6 ± 0.8	$13.1^{+0.7}_{-0.7}$	749^{+69}_{-66}	$3.62^{+0.42}_{-0.40}$	22.3 ± 2.3	$21.2^{+1.2}_{-1.4}$	$120.0^{+16.1}_{-10.9}$	$1.43^{+0.32}_{-0.26}$

interface—affecting the accuracy of the impedance matching calculation. As a result, shots displaying this behavior were not used further in evaluating the equation of state.

IV. RESULTS AND DISCUSSION

A. Shock variables

The experimental data and corresponding calculated shock states are provided in Table II, and the foam Hugoniot data is displayed in Fig. 8 in the (u_p, P) plane. The error bars (calculated from the MC uncertainty) are relatively large: while this uncertainty includes contributions from the error in the quartz Hugoniot, it is dominated by the relatively large measurement error in the quartz and foam shock timings. This is compared to theoretical Hugoniot data from the SESAME 7592 (CH) table [45], along with QEOS [46] data for both CH and TMPTA. All three theoretical Hugoniots correspond to the homogeneous material (i.e., not a foam) at the 260 mg/cm^3 foam density. The QEOS data is produced using the HUGONIOT utility packaged with the radiation hydrodynamics code HYADES [47].

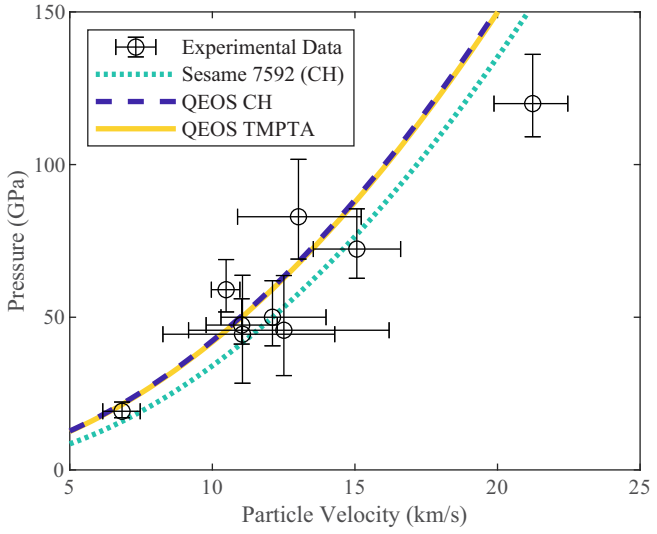

FIG. 8. Experimental u_p-P data compared to principal Hugoniots generated from a range of EOS models. The error bars come from a MC analysis of 10 000 random samples (these error bars are symmetric around the mean of the distribution, which is slightly different from the value calculated through the "exact" calculation—leading to the asymmetry).

It is clear that all three theoretical Hugoniots do a good job of representing the compression behavior of the experimental data. The two QEOS Hugoniots show that there is little difference in compression behavior between CH and TMPTA models, suggesting that it is reasonable to approximate TMPTA foam using CH—and thus the comparison with SESAME 7592 is a valid one (no SESAME table is available for TMPTA). As such this appears to suggest that, in this pressure range, the compression behavior of this foam can be reasonably described by approximating it as a low-density homogeneous plastic.

Figure 9 includes data from previous experiments for other low-density foam materials. These include explosively driven experiments performed on CH at Los Alamos [23], absolute Hugoniot measurements on CH (with a ∼1 μm pore size) using the NRL's Nike laser facility [24], and impedance matched TMPTA-plastic foam experiments (with a ∼0.5 μm pore size) performed at the LULI at Ecole Polytechnique [25]. This plot shows good agreement between the data sets, displaying three separate curves corresponding to the different densities of foam. From comparing the data for foams above 200 mg/cm^3 to the EOS models, it appears that the SESAME model gives the best fit over the full range of pressures represented by the four experiments. The same data could also be considered in terms of density versus pressure. However, density is particularly sensitive to the uncertainty in the data, leading to large relative errors in this value [48]—resulting in large scatter for all of the considered datasets and preventing useful discrimination between models when viewing the current data sets in this format.

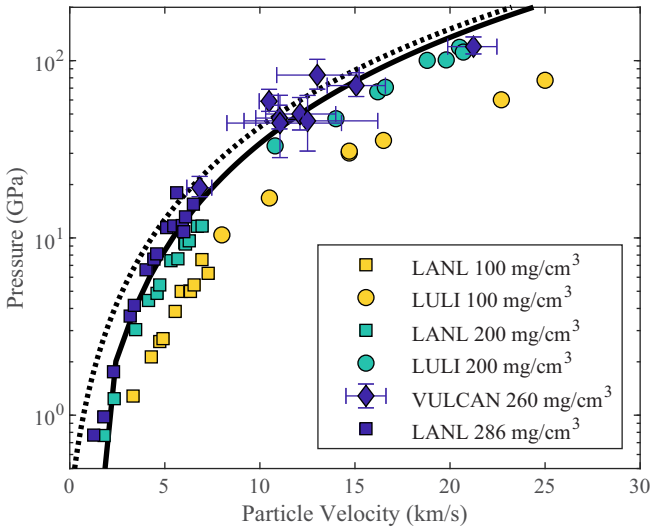

FIG. 9. u_p-P experimental data from a series of experiments on low-density foams. The SESAME and QEOS CH Hugoniots are displayed as the solid and dashed lines respectively (the TMPTA QEOS overlaps the CH QEOS, and so has been omitted). Error bars are displayed for the VULCAN data (but omitted from other sets due to data availability and visibility). Color indicates foam density, while shape indicates the source of the data. The NRL data is at higher particle velocity and pressure and so does not appear on these axes, but continues the trend for the 100 mg/cm^3 data.

B. Temperature data

The temperature data corresponding to the valid shots are displayed in Fig. 10. There are fewer data points in this figure, as the SOP diagnostic did not return useful data for some of the shots. The errors are large due to the on-shot calibration, the shock velocity errors (which propagate through the calculations), and the need for models to estimate the quartz temperature and quartz and foam reflectivities.

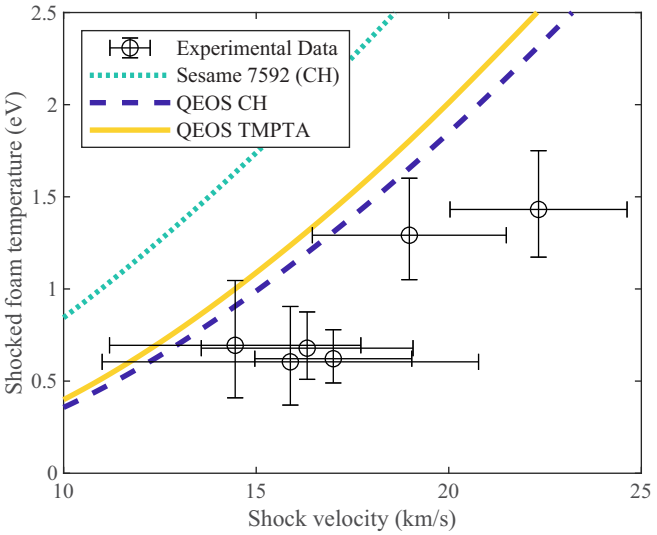

FIG. 10. Gray-body temperature for the shocked foam as a function of shock velocity. Despite the large error bars, the theoretical models are not within the uncertainty of most shots.

The detected signal from the foam was relatively weak, and thus high gain was required on the streak camera to detect it. The resulting signal was quite patchy, and thus firm conclusions can not be drawn from this data with confidence. However, it appears that the foam shock temperatures measured in the experiment were noticeably lower those predicted by the theoretical models, and in particular those suggested by the SESAME data. Despite the large uncertainty in these measurements, the SESAME model does not pass through the error-bars of any of the data points. This could be indicative that such a model overestimates the temperature in this pressure range, although the low signal means that further investigation of this (with a more accurate SOP diagnostic) would be required to make this conclusion with any certainty.

C. Comparison with simulation

One- and two-dimensional radiation hydrodynamic simulations were performed of the experiment in a range of codes (HYADES [47], HELIOS [49], MULTI-1D [50], and FLASH [51,52] were used for 1D simulations, while h2d [53], FLASH, and MULTI-2D [54] were used for 2D). Simulations before the experiment were used to aid target and experiment design, while post-experiment simulations using the measured target dimensions and laser profiles attempted to match the measured data. Figure 11 shows the results from a post-experiment 2D FLASH simulation. This simulation included the foam step and demonstrates that this 2D structure did not significantly change the shock dynamics from the 1D simulations, while also allowing the transit time through each layer to be determined. The simulations also indicated that the ablation front remained in the ablator layer, and thus the gold and quartz were not directly ablated by the laser.

The shock transit time through the different layers of the target were investigated in these simulations, and compared with the experimental results. Figure 12 shows these simulated transit times as a function of intensity (and thus shock strength) for a number of different codes (all simulating the same experimental shot, using the real target dimensions and laser profile). Two transit times are recorded, corresponding to measurements that were made during the experiment: the quartz transit time was identified from the VISAR data, while the combined ablator-gold transit time was determined (with larger uncertainty) as the time difference between the laser being applied, estimated from a fiducial, and the shock entering the quartz layer. It is clear from Fig. 12 that it is not possible to match both experimentally measured transit times in a single simulation. The ablator-gold transit time requires a higher laser intensity, comparable to the $\sim 1.8 \times 10^{14}$ W/cm^2 used in the experiment. However, matching the quartz transit time requires a laser intensity in the simulation that is almost an order of magnitude lower than what was actually used. This discrepancy was observed in every simulation code and in all shots (to varying extent), and suggests that the shock in the quartz is significantly weaker than would be expected based on both the shock strength in the previous layers, and the applied laser intensity. This decreased shock strength in the quartz resulted in much lower pressures than predicted, which explains why VISAR fringe curvature (which requires a

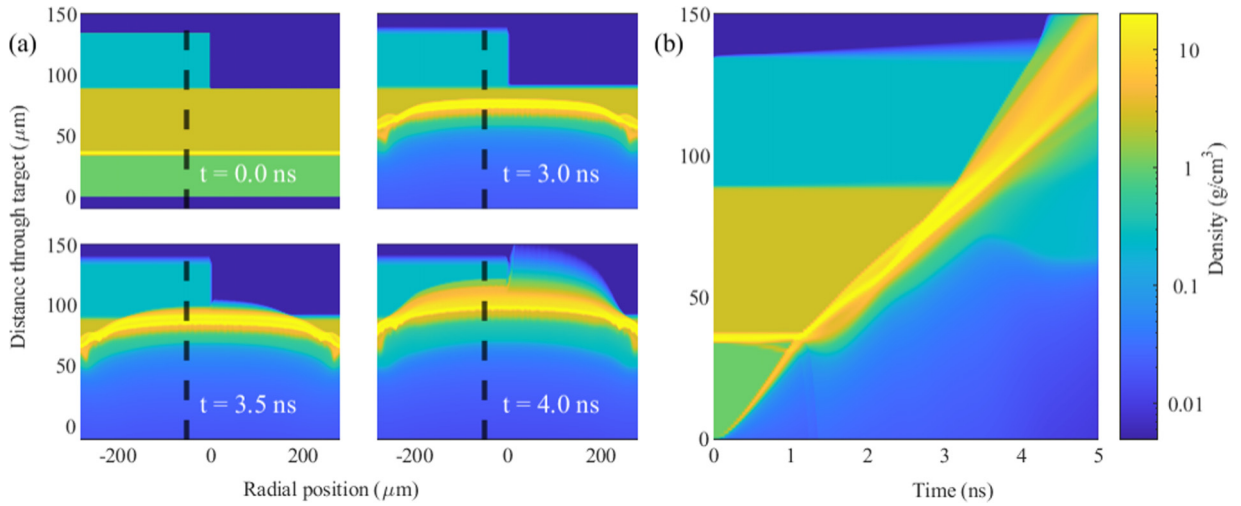

FIG. 11. 2D FLASH simulation using measured target dimensions and temporal laser profile, with a peak laser intensity of 1.8×10^{14} W/cm^2. Panel (a) shows four snapshots of the shock propagating through the target in 2D. It can be seen that the shock propagation through the foam is largely undisturbed by the step structure. Panel (b) shows the shock propagation vs time at a single horizontal position (50 μm within the foam step, indicated by the dashed black line in (a)). The same color scale (representing density) is used in all plots.

minimum pressure to generate a reflective shock in the quartz) was not typically seen.

In a small number of targets, the gold and ablator layers delaminated from the quartz and thus had to be glued on. These targets could not be used in the final results (as the glue layer prevented accurate determination of the quartz shock velocity). However, it was observed that in these targets, the shock strength in the quartz was much closer to that in the ablator, and thus showed better agreement with the simulations (although there was still a discrepancy). The stronger shock strength in the quartz in these targets was also indicated by the fact that some fringe motion was observed in these targets (although the signal strength was too weak for velocities to be determined from this). In fact, all four targets with glue layers which returned analysable data displayed some evidence of fringe motion. This suggests that the shots with glue layers were disproportionately likely compared to the other shots to return a strong shock in the quartz.

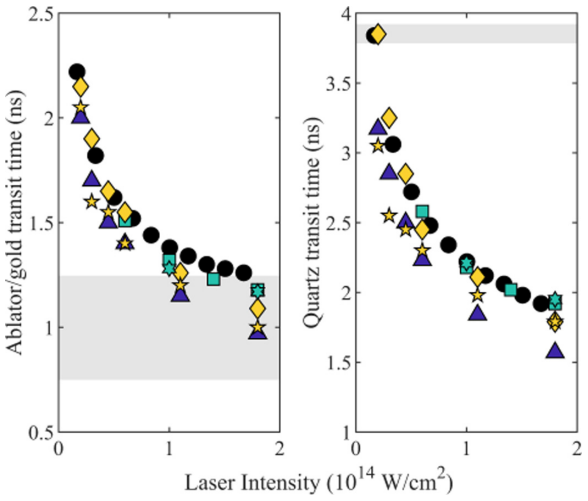

FIG. 12. Simulated shock transit times through the combined ablator and gold layers (left) and the quartz layer (right) for one of the experimental shots. This was performed in 4 different 1D radiation hydrodynamics codes: HYADES (black circles), FLASH (teal squares), MULTI (yellow diamonds), and HELIOS (blue triangles). 2D simulations were also performed in MULTI (yellow stars) and FLASH (teal hexagrams). On each plot, the gray shaded region corresponds to the experimentally measured value (bounded by the uncertainty). The agreement between codes is good, and in all cases it is not possible to match the experimentally measured times in both ablator-gold and quartz layers at any one intensity.

It is therefore apparent that adding the glue layer appeared to reduce the observed discrepancy, and led to a stronger shock in the quartz. Any explanation for the discrepancy in this experiment must therefore explain three observations: (1) that the shock is significantly weaker in the quartz than is expected based on the strength in the ablator and the simulations, (2) that the shock is not substantially weaker in the foam than in the quartz (as might be expected if the shock was continually decaying throughout the transit), and (3) that gluing the gold to the quartz substantially improves the quartz shock strength. Based on these criteria, a possible explanation for this behavior is that there was a partial delamination and poor contact between the gold and quartz layers. The resulting gaps could lead to shock decay between the two layers (explaining the observed discrepancy), but the issue would be improved by gluing the two layers together (explaining the improvement seen for the glue targets). Such delamination is also feasible, as full delamination of some targets did indeed occur (hence the need for the glue layers). Attempts were made to investigate the effect of such a gap in the hydrodynamic simulations, but without success; 1D and 2D simulations with a constant gap between the layers did not result in an increase in shock transit time. However, 2D FLASH simulations where the gap structure was more complicated (and not-constant thickness) did result in a small change. This increase was not particularly significant, but could indicate that for a very nonlinear interface between the layers, as would likely be the case in a real target, that this could be a viable explanation.

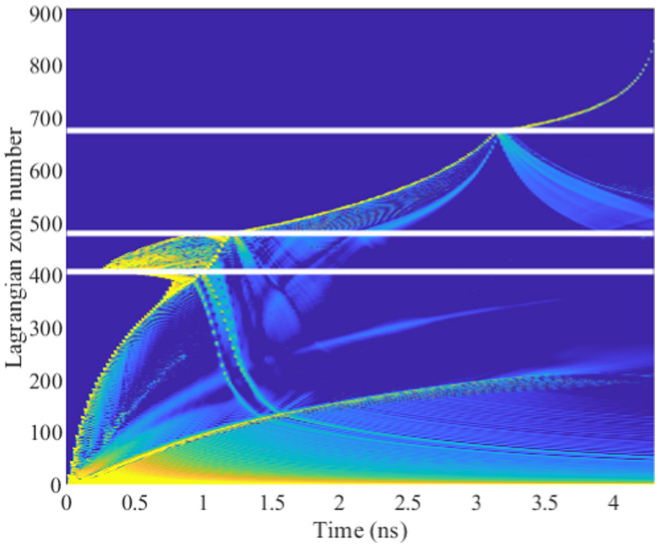

FIG. 13. Shock propagation plot (log-derivative of pressure) from a 1D HYADES simulation of the same shot and laser intensity as in Fig. 11. It can be seen that a second shock (originating from the gold layer) catches and overtakes the primary shock just before it reaches the foam layer (this is different to the FLASH simulation, where this occurs at an earlier time). The figure is plotted as a function of Lagrangian simulation zone number (rather than radius), so that the zone and material boundaries are stationary and the shock propagation can be seen more easily. The material interfaces are indicated by the white horizontal lines.

It is important to note that this discussion relates to the discrepancy between the experiment and the simulation efforts, but does not impact the validity of the results presented in Sec. IV. These results simply require that a steady shock passes through the quartz and foam, and is not concerned if this shock is weaker than expected. The shock variables are not measured until after the shock has entered the quartz (a time which can clearly be well identified in the raw data, as seen in Fig. 3), and thus any behavior in the preceding layers will not have any effect on the results and analysis.

The simulations also allow two potential sources of systematic error to be investigated. First (and as discussed in Sec. III C), there is an additional shock generated when the shock wave first crosses the gold-quartz interface. This shock backward-propagates through the target before reflecting from the ablation front. In some cases this second shock can catch and overtake the first shock, which would impact the accuracy of the calculated shock velocities and thus the impedance matching calculation. This phenomena can be observed in Fig. 11 (where the shock merger is seen at ∼2.5 ns), or more clearly in Fig. 13, where it occurs just before the shock reaches the foam boundary. These two simulations are of the same shot and conditions, but in 2D FLASH and 1D HYADES, and demonstrate that this effect exhibits significant differences between simulation codes (a HELIOS simulation of the same shot showed even greater difference, with the merger occurring just as the shock breaks out from the rear of the target). This behavior cannot be accurately simulated, since (a) the decrease in shock strength between the combined ablator and gold and the quartz would likely also affect the second shock to an unknown extent, and (b) uncertainty around the first shock will lead to greater uncertainty regarding the second, as the second shock travels through already shocked material. Potential evidence of a second shock was seen in some of the experimental shots, but as discussed in Sec. III C these shots were then omitted from the final results. As a result, it is thought to be unlikely that this had a significant impact on the experimental results.

The second potential source of systematic error is the shock stability. Impedance matching requires knowledge of the shock velocity in the quartz just before it crosses the quartz-foam boundary, and the shock velocity in the foam just after. The use of average shock velocities in this experiment therefore requires that these average values are a reasonable approximation of the velocities at these times; if the shock is decaying, then this is not the case and this would result in a systematic error. It had been intended that the shock velocity as a function of time could be measured using the VISAR, but the lack of observed fringe motion prohibited this.

Simulations indicated some degree of shock decay was present, but that the average shock velocity measurements used are likely sufficient to give a reasonable estimate of the achieved shock states (although it should be noted that the shock stability could also be influenced by the unexpected decrease in shock strength between ablator and quartz, which is not captured in these simulations). Figure 14 shows the shock velocity, pressure and particle velocity at the shock front from a 1D HELIOS simulation (a 1D simulation was used for this analysis to enable high resolution for accurate shock front tracking) using the same real target dimensions and laser profile as Fig. 11, at a lower intensity intended to give a more accurate quartz transit. It can be seen that the shock is reasonably stable in the quartz (with a small amount of decay), and slightly less stable in the foam. The dashed horizontal lines on the shock velocity plots represents the average shock velocity that would be calculated from the transit times and layer thicknesses, and it can be seen that this is a reasonable approximation in both materials. These average shock velocities were then analysed in the same way as the real experimental data, giving the dashed horizontal lines seen in the pressure and particle velocity plots. While there is some difference to the true shock states (ideally this would match the final shock profile in the quartz, and the first shock profile in the foam), the calculated quantities are a reasonable approximation of the true values. This suggests that the use of average velocity measurements in this experiment was likely valid (with the systematic error introduced by this estimated at around 10%, which is typically less that the random error represented by the error bars).

D. Suggested improvements

If this subject were to be further investigated, there are a number of potential improvements that could be made. Given the proposed gap between the gold and quartz layers, the importance of improved target fabrication and metrology is emphasised—if this experiment was to be repeated, x-ray diagnostics could be used to test for delamination in these targets. Alternatively, the ablator layer could be doped with a material such as iodine or bromine to prevent preheating [55],

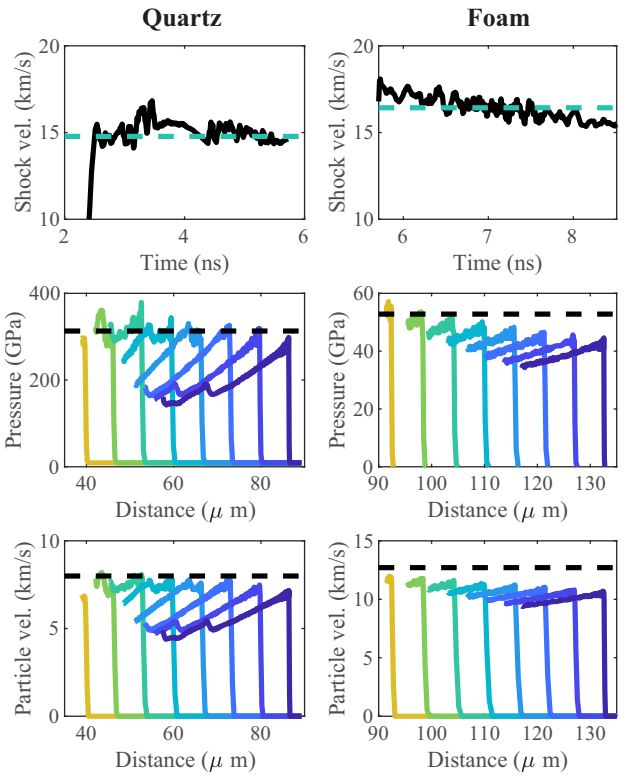

FIG. 14. Simulated shock velocity, pressure and particle velocity at the shock front as the shock propagates through the quartz and foam layers, from a 1D HELIOS simulation with a laser intensity of 1.5×10^{13} W/cm^2. The shock velocity is displayed as a function of time, while for pressure and particle velocity, profiles of the shock front are provided at eight equally spaced time intervals (later times are further to the right, and are plotted in darker color). The shock transit times through the quartz and the foam were used to calculate average shock velocities (the dashed horizontal teal lines). The same analysis procedure as used on the experimental data was then used to calculate the pressure and particle velocity in the two materials (the dashed horizontal black lines).

removing the need for the gold layer. This ablator layer could be formed of an undoped layer followed by a doped layer, to prevent the heavier ions from radiating under direct laser heating. Replacing the gold layer would simplify the target, potentially reduce the risk of delamination, and could also help prevent the generation of the second shock discussed in Sec. III C—removing a source of uncertainty. If a stronger shock could be achieved in the quartz, then it should be possible to determine the shock velocity as a function of time in this layer using the VISAR, which would both remove the need to use the average velocity in this layer and enable the shock stability to be determined. Alternatively, the quartz could be replaced with a material which exhibits shock reflectivity at a lower pressure, so that the VISAR could be utilised in this manner in the current pressure regime.

Changes could be made to the implementation of the experiment to improve performance. First, a more sensitive streaked optical pyrometer could be used. Using a more sensitive streak camera would yield improved signal strength, which would enable the temperature to be estimated more accurately and with more confidence. Ideally this SOP should be absolutely calibrated, so that the temperature can be measured without assuming a temperature for the quartz. Improvements could also be achieved by using a simpler optical relay, consisting of a shorter optical path with fewer components. This would result in an easier setup and also hopefully lead to less loss of light, which would benefit the signal strength for both the VISAR and the SOP. [The more complicated setup used in this experiment was due to early attempts to inject the probe laser through the VISAR beamsplitter (component "k" in Fig. 1), so that one fewer beamsplitter was required (as component "d" could therefore be a mirror); doing so resulted in the focusing of the probe laser at the target and thus poor illumination over the VISAR/SOP field of view, necessitating the change to the setup presented in this paper.]

V. CONCLUSIONS

Principal Hugoniot data for TMPTA foam at a density of 260 mg/cm^3 was successfully measured in an impedance matching experiment and found to be in reasonable agreement with theoretical Hugoniots predicted using the CH and TMTPA QEOS models and the SESAME 7592 table. These theoretical Hugoniots all assume the foam to be a low-density homogeneous plastic, suggesting that this assumption can be used to describe the compression behavior of the foam to reasonable accuracy. The temperature of the shocked foam was also estimated based on self-emission, and this data appeared to suggest that the existing EOS models (particularly the SESAME data) over-estimated the foam temperature. However this SOP data was of low signal-to-noise ratio (and the lack of absolute calibration led to large uncertainties), which means that further investigation is required to confirm these temperature-based findings.

This data was also compared to previous experiments looking at low-density foams. It was found that generally this data fit the trends observed in those experiments. Comparison of the different theoretical Hugoniots over a wider pressure range again confirmed that they were a reasonable description of such foams, with closest agreement found to the SESAME data. Overall, the comparison with previous experiments is encouraging, and confirms the conclusion that this material is well described with a low-density homogeneous plastic equation of state.

ACKNOWLEDGMENTS

© British Crown Copyright 2023/AWE. The authors gratefully acknowledge P. Oliveira, D. Pepler, D. Wyatt, and the rest of the staff of the Central Laser Facility for their assistance with the experiment, as well as computing resources provided by the STFC Scientific Computing Department's SCARF cluster. They also thank R. Bingham, S. Le Pape, O. Rosmej, and G. Kagan for useful discussions. R.W.P. acknowledges funding from UKRI-EPSRC and AWE-plc through his Industrial CASE scholarship. M.v.d.L., R.A., and P.A.N. acknowledge support from STFC Grants No. ST/T001933/1 and No. ST/V001655/1 and the Oxford-ShanghaiTech collaboration agreement. This work has been

carried out within the framework of the EUROfusion Consortium, funded by the European Union via the Euratom Research and Training Programme (Grant Agreement No. 101052200–EUROfusion). Views and opinions expressed are however those of the author(s) only and do not necessarily reflect those of the European Union or the European Commission. Neither the European Union nor the European Commission can be held responsible for them.

[1] S. Depierreux, C. Labaune, D. T. Michel, C. Stenz, P. Nicolaï, M. Grech, G. Riazuelo, S. Weber, C. Riconda, V. T. Tikhonchuk, P. Loiseau, N. G. Borisenko, W. Nazarov, S. Hüller, D. Pesme, M. Casanova, J. Limpouch, C. Meyer, P. DiNicola, R. Wrobel *et al.*, Phys. Rev. Lett. **102**, 195005 (2009).

[2] S. X. Hu, W. Theobald, P. B. Radha, J. L. Peebles, S. P. Regan, A. Nikroo, M. J. Bonino, D. R. Harding, V. N. Goncharov, N. Petta, T. C. Sangster, and E. M. Campbell, Phys. Plasmas **25**, 082710 (2018).

[3] R. S. Craxton, K. S. Anderson, T. R. Boehly, V. N. Goncharov, D. R. Harding, J. P. Knauer, R. L. McCrory, P. W. McKenty, D. D. Meyerhofer, J. F. Myatt, A. J. Schmitt, J. D. Sethian, R. W. Short, S. Skupsky, W. Theobald, W. L. Kruer, K. Tanaka, R. Betti, T. J. Collins, J. A. Delettrez *et al.*, Phys. Plasmas **22**, 110501 (2015).

[4] S. E. Bodner, D. G. Colombant, J. H. Gardner, R. H. Lehmberg, S. P. Obenschain, L. Phillips, A. J. Schmitt, J. D. Sethian, R. L. McCrory, W. Seka, C. P. Verdon, J. P. Knauer, B. B. Afeyan, and H. T. Powell, Phys. Plasmas **5**, 1901 (1998).

[5] T. J. Collins, A. Poludnenko, A. Cunningham, and A. Frank, Phys. Plasmas **12**, 062705 (2005).

[6] S. Skupsky, J. A. Marozas, R. S. Craxton, R. Betti, T. J. Collins, J. A. Delettrez, V. N. Goncharov, P. W. McKenty, P. B. Radha, T. R. Boehly, J. P. Knauer, F. J. Marshall, D. R. Harding, J. D. Kilkenny, D. D. Meyerhofer, T. C. Sangster, and R. L. McCrory, Phys. Plasmas **11**, 2763 (2004).

[7] W. Shang, R. Yu, W. Zhang, and J. Yang, Nucl. Fusion **56**, 086002 (2016).

[8] R. E. Olson, R. J. Leeper, J. L. Kline, A. B. Zylstra, S. A. Yi, J. Biener, T. Braun, B. J. Kozioziemski, J. D. Sater, P. A. Bradley, R. R. Peterson, B. M. Haines, L. Yin, L. F. Berzak Hopkins, N. B. Meezan, C. Walters, M. M. Biener, C. Kong, J. W. Crippen, G. A. Kyrala *et al.*, Phys. Rev. Lett. **117**, 245001 (2016).

[9] A. B. Zylstra, S. A. Yi, B. M. Haines, R. E. Olson, R. J. Leeper, T. Braun, J. Biener, J. L. Kline, S. H. Batha, L. Berzak Hopkins, S. Bhandarkar, P. A. Bradley, J. Crippen, M. Farrell, D. Fittinghoff, H. W. Herrmann, H. Huang, S. Khan, C. Kong, B. J. Kozioziemski *et al.*, Phys. Plasmas **25**, 056304 (2018).

[10] R. E. Olson, M. J. Schmitt, B. M. Haines, G. E. Kemp, C. B. Yeamans, B. E. Blue, D. W. Schmidt, A. Haid, M. Farrell, P. A. Bradley, H. F. Robey, and R. J. Leeper, Phys. Plasmas **28**, 122704 (2021).

[11] B. M. Haines, S. A. Yi, R. E. Olson, S. F. Khan, G. A. Kyrala, A. B. Zylstra, P. A. Bradley, R. R. Peterson, J. L. Kline, R. J. Leeper, and R. C. Shah, Phys. Plasmas **24**, 072709 (2017).

[12] R. W. Paddock, H. Martin, R. T. Ruskov, R. H. H. Scott, W. Garbett, B. M. Haines, A. B. Zylstra, R. Aboushelbaya, M. W. Mayr, B. T. Spiers, R. H. W. Wang, and P. A. Norreys, Philos. Trans. R. Soc. A **379**, 20200224 (2021).

[13] B. M. Haines, R. E. Olson, W. Sweet, S. A. Yi, A. B. Zylstra, P. A. Bradley, F. Elsner, H. Huang, R. Jimenez, J. L. Kline, C. Kong, G. A. Kyrala, R. J. Leeper, R. Paguio, S. Pajoom, R. R. Peterson, M. Ratledge, and N. Rice, Phys. Plasmas **26**, 012707 (2019).

[14] V. N. Goncharov, I. V. Igumenshchev, D. R. Harding, S. F. B. Morse, S. X. Hu, P. B. Radha, D. H. Froula, S. P. Regan, T. C. Sangster, and E. M. Campbell, Phys. Rev. Lett. **125**, 065001 (2020).

[15] G. Hazak, A. L. Velikovich, J. H. Gardner, and J. P. Dahlburg, Phys. Plasmas **5**, 4357 (1998).

[16] M. Cipriani, S. Y. Gus'kov, F. Consoli, R. De Angelis, A. A. Rupasov, P. Andreoli, G. Cristofari, G. Di Giorgio, and M. Salvadori, High Power Laser Science and Engineering **9**, e40 (2021).

[17] M. Cipriani, S. Y. Gus'Kov, R. De Angelis, F. Consoli, A. A. Rupasov, P. Andreoli, G. Cristofari, G. Di Giorgio, and F. Ingenito, Laser Part. Beams **36**, 121 (2018).

[18] J. Colvin and J. Larsen, *Extreme Physics* (Cambridge University Press, Cambridge, 2013).

[19] Ph. Nicolaï, M. Olazabal-Loumé, S. Fujioka, A. Sunahara, N. Borisenko, S. Gus'Kov, A. Orekov, M. Grech, G. Riazuelo, C. Labaune, J. Velechowski, and V. Tikhonchuk, Phys. Plasmas **19**, 113105 (2012).

[20] K. Falk, L. A. Collins, E. J. Gamboa, G. Kagan, J. D. Kress, D. S. Montgomery, B. Srinivasan, P. Tzeferacos, and J. F. Benage, Phys. Plasmas **21**, 056309 (2014).

[21] K. Falk, C. A. Mccoy, C. L. Fryer, C. W. Greeff, A. L. Hungerford, D. S. Montgomery, D. W. Schmidt, D. G. Sheppard, J. R. Williams, T. R. Boehly, and J. F. Benage, Phys. Rev. E **90**, 033107 (2014).

[22] K. Falk, C. J. Fontes, C. L. Fryer, C. W. Greeff, M. Holec, H. M. Johns, D. S. Montgomery, D. W. Schmidt, and M. Šmíd, Plasma Phys. Control. Fusion **62**, 074001 (2020).

[23] S. P. Marsh (ed.), *Los Alamos Series on Dynamic Material Properties* (University of California Press, Berkeley/Los Angeles, CA, 1980), p. 150.

[24] Y. Aglitskiy, A. L. Velikovich, M. Karasik, A. J. Schmitt, V. Serlin, J. L. Weaver, J. Oh, S. P. Obenschain, and K. R. Cochrane, Phys. Plasmas **25**, 032705 (2018).

[25] M. Koenig, A. Benuzzi, F. Philippe, D. Batani, T. Hall, N. Grandjouan, and W. Nazarov, Phys. Plasmas **6**, 3296 (1999).

[26] R. W. Paddock, H. Martin, R. T. Ruskov, R. H. H. Scott, W. Garbett, B. M. Haines, A. B. Zylstra, E. M. Campbell, T. J. B. Collins, R. S. Craxton, C. A. Thomas, V. N. Goncharov, R. Aboushelbaya, Q. S. Feng, M. W. Von Der Leyen, I. Ouatu, B. T. Spiers, R. Timmis, R. H. W. Wang, and P. A. Norreys, J. Plasma Phys. **88**, 905880314 (2022).

[27] J. Biener, C. Dawedeit, S. H. Kim, T. Braun, M. A. Worsley, A. A. Chernov, C. C. Walton, T. M. Willey, S. O. Kucheyev, S. J. Shin, Y. M. Wang, M. M. Biener, J. R. Lee, B. J. Kozioziemski, T. Van Buuren, K. J. Wu, J. H. Satcher, and A. V. Hamza, Nucl. Fusion **52**, 062001 (2012).

[28] T. Braun, S. H. Kim, M. M. Biener, A. V. Hamza, and J. Biener, Fusion Sci. Technol. **73**, 229 (2018).
[29] L. M. Barker, AIP Conf. Proc. **505**, 11 (2000); L. M. Barker and R. E. Hollenbach, J. Appl. Phys. **43**, 4669 (1972).
[30] D. G. Hicks, T. R. Boehly, J. H. Eggert, J. E. Miller, P. M. Celliers, and G. W. Collins, Phys. Rev. Lett. **97**, 025502 (2006).
[31] P. M. Celliers, D. K. Bradley, G. W. Collins, D. G. Hicks, T. R. Boehly, and W. J. Armstrong, Rev. Sci. Instrum. **75**, 4916 (2004).
[32] M. D. Knudson and M. P. Desjarlais, Phys. Rev. B **88**, 184107 (2013).
[33] Y. B. Zel'dovich and Y. P. Raizer, *Physics of Shock Waves and High-Temperature Hydrodynamic Phenomena*, edited by W. D. Hayes and R. F. Probstein (Academic Press, New York, NY, 1966).
[34] M. D. Knudson and M. P. Desjarlais, Phys. Rev. Lett. **103**, 225501 (2009).
[35] D. G. Hicks, T. R. Boehly, P. M. Celliers, D. K. Bradley, J. H. Eggert, R. S. McWilliams, R. Jeanloz, and G. W. Collins, Phys. Rev. B **78**, 174102 (2008).
[36] D. G. Hicks, T. R. Boehly, P. M. Celliers, J. H. Eggert, E. Vianello, D. D. Meyerhofer, and G. W. Collins, Phys. Plasmas **12**, 082702 (2005).
[37] R. F. Trunin, Phys. Usp. **37**, 1123 (1994).
[38] J. W. Forbes, *Shock Wave Compression of Condensed Matter: A Primer* (Springer, Berlin, 2012), pp. 1–374.
[39] S. Root, R. J. Magyar, J. H. Carpenter, D. L. Hanson, and T. R. Mattsson, Phys. Rev. Lett. **105**, 085501 (2010).
[40] M. C. Gregor, R. Boni, A. Sorce, J. Kendrick, C. A. McCoy, D. N. Polsin, T. R. Boehly, P. M. Celliers, G. W. Collins, D. E. Fratanduono, J. H. Eggert, and M. Millot, Rev. Sci. Instrum. **87**, 114903 (2016).
[41] J. E. Miller, T. R. Boehly, A. Melchior, D. D. Meyerhofer, P. M. Celliers, J. H. Eggert, D. G. Hicks, C. M. Sorce, J. A. Oertel, and P. M. Emmel, Rev. Sci. Instrum. **78**, 034903 (2007).
[42] M. Millot, N. Dubrovinskaia, A. Černok, S. Blaha, L. Dubrovinsky, D. G. Braun, P. M. Celliers, G. W. Collins, J. H. Eggert, and R. Jeanloz, Science **347**, 418 (2015).
[43] S. X. Hu, T. R. Boehly, and L. A. Collins, Phys. Rev. E **89**, 063104 (2014).
[44] S. X. Hu, L. A. Collins, J. P. Colgan, V. N. Goncharov, and D. P. Kilcrease, Phys. Rev. B **96**, 144203 (2017).
[45] S. P. Lyon and J. D. Johnson, SESAME 7592, in Los Alamos National Laboratory Report No. LA-UR-92-3407 (1995).
[46] R. M. More, K. H. Warren, D. A. Young, and G. B. Zimmerman, Phys. Fluids **31**, 3059 (1988).
[47] J. T. Larsen and S. M. Lane, J. Quant. Spectrosc. Radiat. Transfer **51**, 179 (1994).
[48] S. Le Pape, A. MacPhee, D. Hey, P. Patel, A. MacKinnon, M. Key, J. Pasley, M. Wei, S. Chen, T. Ma, F. Beg, N. Alexander, R. Stephens, D. Offerman, A. Link, L. Van-Woerkom, and R. Freeman, Rev. Sci. Instrum. **79**, 106104 (2008).
[49] J. J. MacFarlane, I. E. Golovkin, and P. R. Woodruff, J. Quant. Spectrosc. Radiat. Transfer **99**, 381 (2006).
[50] R. Ramis, R. Schmalz, and J. Meyer-Ter-Vehn, Comput. Phys. Commun. **49**, 475 (1988).
[51] B. Fryxell, K. Olson, P. Ricker, F. X. Timmes, M. Zingale, D. Q. Lamb, P. MacNeice, R. Rosner, J. W. Truran, and H. Tufo, Astrophy. J. Suppl. Ser. **131**, 273 (2000).
[52] A. Dubey, K. Antypas, M. K. Ganapathy, L. B. Reid, K. Riley, D. Sheeler, A. Siegel, and K. Weide, Parallel Comput. **35**, 512 (2009).
[53] h2d is a commercial product of Cascade Applied Sciences Incorporated, 6325 Trevarton Drive, Longmont, CO, 80503, USA (e-mail: Larsen@casinc.com).
[54] R. Ramis, J. Meyer-ter Vehn, and J. Ramírez, Comput. Phys. Commun. **180**, 977 (2009).
[55] T. R. Desjardins, C. A. Di Stefano, E. C. Merritt, K. A. Flippo, and F. W. Doss, High Energy Den. Phys. **39**, 100937 (2021).